Research Square

Preprints are preliminary reports that have not undergone peer review.
They should not be considered conclusive, used to inform clinical practice,
or referenced by the media as validated information.

Delamination configuration-induced compressive failure evolution and load-carrying degradation mechanisms of wind turbine blade spar-cap laminates

Wenhu Gu
Hohai University
Xin Cai
xcai@hhu.edu.cn

Hohai University
Qinghui Liu
Hohai University
Min Li
Hohai University
Yanan Zhang
Hohai University

Research Article

Keywords: Wind turbine blade, Spar-cap laminate, Delamination, Interfacial damage, Load-carrying capacity

Posted Date: November 9th, 2026

DOI: https://doi.org/10.21203/rs.3.rs-11471491/v1

License: This work is licensed under a Creative Commons Attribution 4.0 International License.
Read Full License

Additional Declarations: No competing interests reported.

Delamination configuration-induced compressive failure evolution and load-carrying degradation mechanisms of wind turbine blade spar-cap laminates

Wenhu Gu[a b], Xin Cai[a c *], Qinghui Liu[a], Min Li[a d], Yanan Zhang[e]

[a] College of Mechanics and Engineering Science, Hohai University, Nanjing, 211100, China

[b] Faculty of Architecture and Civil Engineering, Huai'an University, Huai'an, 223003, China

[c] Jiangsu Province Engineering Research Center of Wind Turbine Structures, Hohai University, Nanjing, 211100, China

[d] National Technology Innovation Center for Wind Power, Hohai University, Nanjing, 211100, China

[e] College of Water Conservancy and Hydropower Engineering, Hohai University, Nanjing, 210098, China

[*] Corresponding author. E-mail address: xcai@hhu.edu.cn

Abstract: Delamination-induced local instability, damage evolution, and compressive load degradation are critical issues affecting the structural performance of wind turbine blade spar-cap laminates. In this study, a three-dimensional nonlinear finite element model incorporating matrix nonlinearity, intralaminar progressive damage, and interfacial delamination propagation was developed to investigate the effects of delamination configurations on compressive failure evolution and load-carrying capacity. The influences of delamination size, through-thickness position, and multiple-delamination spatial configuration were systematically examined. The results show that initial delamination reduces local interlaminar constraint, triggering sub-laminate buckling and subsequently promoting interfacial damage propagation and load-transfer degradation. Increasing delamination size continuously decreases the ultimate load-carrying capacity, whereas moving the delamination toward the laminate mid-plane improves local stability by balancing the bending stiffness of the separated sub-laminates. For multiple delaminations, increasing the in-plane spacing between coplanar delaminations partially restores the constraint and load-transfer capability of the intact material region, while overlapping delaminations exhibit a pronounced non-monotonic through-thickness spacing effect. These effects can be attributed to the changes in effective unconstrained length, sub-laminate stiffness distribution, and spatial constraint interactions among multiple defects, which collectively govern local buckling, interfacial damage evolution, and final load degradation. The findings provide mechanistic insights into the assessment of delamination-induced damage and residual load-carrying capability of composite wind turbine blade structures.

Keywords: Wind turbine blade; Spar-cap laminate; Delamination; Interfacial damage; Load-carrying capacity

Highlights:

- A coupled 3D model links matrix nonlinearity, intralaminar damage and delamination.
- Delamination size and position govern compression through local stability changes.
- Coplanar spacing controls local constraint recovery and residual load capacity.
- Overlapping delaminations exhibit a non-monotonic through-thickness spacing effect.
- A unified mechanism links delamination configuration, buckling, damage and capacity loss.

1 Introduction

Wind turbine blades are key load-carrying components responsible for energy capture and load transfer in wind energy systems, and their structural development is increasingly driven by the

demands for larger dimensions and lower structural weight [1,2]. Owing to their high specific strength and stiffness, fiber-reinforced composites have become the primary materials used in major load-bearing regions of blades, including the spar caps, shear webs, and skins [3]. Among these components, the spar cap primarily carries the axial tensile and compressive stresses induced by blade bending, making its local stability and damage tolerance critical to structural integrity [4]. During manufacturing, transportation, and long-term service, laminated composite structures may develop various internal defects, including delamination, debonding, voids, and wrinkles, among which delamination is one of the most detrimental interlaminar damage modes affecting compressive performance [5]. Under compressive loading, delamination weakens the through-thickness constraint between adjacent plies, alters the local stability of the separated sub-laminates, and may trigger local out-of-plane buckling. The sequence of local and global buckling depends on the delamination size, through-thickness position, and boundary conditions. As the out-of-plane deformation develops, additional bending and interlaminar stress concentrations arise near the delamination front, which may further promote interfacial damage propagation and degradation of the overall load-carrying capacity [6]. Studies on wind turbine blade spar caps have also shown that the size and through-thickness position of delamination can significantly affect local buckling, damage propagation, and the final failure mode [7–9].

The influence of delamination geometry on the compressive failure of laminated composites has been extensively investigated. Short et al. [10] demonstrated through compression tests and finite element analyses that delamination geometry affects compressive failure by altering the buckling behavior of the delaminated sub-laminate. Calvo et al. [11] combined digital image correlation with finite element analysis to investigate FRP laminates containing delaminations of different sizes and through-thickness positions, showing that delamination geometry significantly modifies local instability and the subsequent failure process. Zhang et al. [12] further examined embedded circular and rectangular delaminations using experiments and progressive damage analysis, and revealed the effects of delamination shape, number, and through-thickness distribution on the compressive response and interfacial damage evolution. Li et al. [13] similarly reported that delamination area and through-thickness position exert a more pronounced influence on the compressive performance of FRP laminates than the shape of the delamination front. More recently, Du et al. [14] showed through compression-after-multiple-impact tests that increasing impact-induced delamination area significantly reduces the residual compressive strength and promotes local out-of-plane buckling of the delaminated sub-laminate, indicating that local stiffness degradation and sub-laminate instability are important factors governing compressive load degradation. Overall, delamination size and through-thickness position not only define the geometric characteristics of the defect, but also modify the effective unsupported length and sub-laminate thickness configuration, thereby altering the local stability conditions of the delaminated region.

Building on these studies, research has progressively evolved from evaluating critical buckling and strength degradation toward characterizing the full process of postbuckling deformation and delamination propagation. Köllner [15] developed an analytical model for buckling-driven delamination growth that accounts for structural coupling, contact, and mixed-mode fracture, and investigated the effects of delamination size and through-thickness position on delamination propagation from the perspective of energy release rate. Shabanijafroudi and Ganesan [16] proposed an analytical framework incorporating buckling, postbuckling, and delamination growth, thereby linking interfacial fracture following local instability to the subsequent postbuckling response. Venkat et al. [17] further demonstrated that delamination size and position can alter the transition

among local buckling, delamination growth, and coupled local–global instability. These studies indicate that, for laminates containing delamination defects, evaluating defect severity solely in terms of buckling load or ultimate strength is insufficient to fully characterize the underlying compressive failure process. It is also necessary to clarify how local sub-laminate buckling evolves into progressive damage, leading to the gradual loss of structural stability and postbuckling load-carrying capacity.

Multiple delaminations may coexist in practical laminated composite structures, making local stability further dependent on the spatial arrangement of defects. Hwang and Liu [18] showed that the number, relative size, and through-thickness distribution of multiple delaminations can significantly alter both the buckling load and buckling mode. Through experimental and finite element investigations, Wang et al. [19] demonstrated that the compressive strength degradation caused by multiple delaminations cannot be interpreted as a simple superposition of individual delamination effects, but is closely related to the thickness configuration of the sub-laminates formed between adjacent delaminations. Jin et al. [20] and Zhu et al. [21] further investigated the buckling and postbuckling behavior of laminates containing multiple delaminations with different lengths and through-thickness positions using theoretical, numerical, and experimental approaches, confirming that the spatial distribution of multiple delaminations has a pronounced influence on structural stability. These studies have provided an important basis for understanding the compressive behavior of laminates with multiple delaminations. However, existing investigations have mainly focused on through-thickness multiple delaminations, defect number, and combinations of delamination length and depth. By contrast, systematic comparisons remain limited for the in-plane spacing effect of discrete coplanar delaminations and the through-thickness configuration effect of overlapping delaminations with coincident in-plane projections. In particular, how their load-carrying responses are governed by the local constraint between neighboring defects and the stiffness configuration of the intermediate sub-laminate remains to be clarified.

Meanwhile, a reliable representation of the aforementioned failure process requires a numerical framework capable of simultaneously capturing geometric instability, intralaminar material nonlinearity, and interlaminar delamination growth. Cohesive zone models have been widely employed to describe the progressive evolution of initially intact interfaces from elastic load transfer to damage initiation and subsequent delamination propagation. De Carvalho and Ratcliffe [22] further developed a cohesive-element formulation that accounts for the directionality of delamination growth. Within individual plies, polymer-matrix composites may exhibit pronounced nonlinear deformation under matrix-dominated transverse and shear stress states prior to the onset of macroscopic damage. The transversely isotropic three-dimensional plasticity model developed by Vogler et al. [23], together with the three-dimensional elastic-plastic damage models proposed by Ding et al. [24] and Goncalves et al. [25], demonstrated that pre-damage matrix nonlinearity can influence local stress redistribution and subsequent damage initiation. Therefore, for delamination-induced compressive instability, considering only interfacial delamination growth or treating the plies as purely linear elastic prior to damage initiation may be insufficient to capture the coupled mechanical feedback among matrix nonlinearity, intralaminar stiffness degradation, and interfacial damage triggered by local buckling.

In summary, previous studies have demonstrated the important effects of delamination size, through-thickness position, and multiple-delamination configurations on the compressive behavior of laminated composites. However, several issues remain insufficiently addressed for representative wind turbine blade spar-cap laminates. First, the effects of delamination size and through-thickness position on local stability and load-carrying performance have often been investigated separately,

while systematic comparisons of different single-delamination geometric parameters within a unified mechanical framework remain limited. Second, the influences of the in-plane and through-thickness spatial configurations of multiple delaminations have not yet been fully clarified, and the resulting differences in load-carrying response still require further interpretation in terms of local constraint conditions and sub-laminate stiffness configuration.

To address these issues, an equivalent laminate representative of a typical wind turbine blade spar-cap region was considered in this study. A nonlinear finite element framework incorporating matrix elastic-plasticity, three-dimensional intralaminar progressive damage, and cohesive interlaminar delamination growth was developed and validated against published compression tests in terms of compressive buckling response and the effect of delamination size. Under consistent material, boundary, and loading conditions, the effects of single-delamination size and through-thickness position, as well as the in-plane spacing of coplanar double delaminations and the through-thickness spacing of overlapping double delaminations, were systematically investigated with respect to compressive load-carrying response, local out-of-plane deformation, and damage evolution. Based on these results, the load-carrying degradation mechanisms associated with different delamination configurations were interpreted in terms of the effective unsupported length, sub-laminate stiffness distribution, and spatial constraint relationships among multiple defects, thereby establishing a physical link between delamination configuration and ultimate load-carrying performance.

2 Numerical methodology and model validation

2.1 Coupled intralaminar-interlaminar damage framework

Fiber-reinforced composite laminates exhibit pronounced nonlinear behavior under compressive loading. Prior to damage initiation, the fiber-dominated longitudinal response generally retains a high stiffness and remains approximately linear elastic, whereas matrix-dominated transverse normal and shear responses may undergo noticeable elastic-plastic deformation and irreversible response before the formation of macroscopic cracks. Treating all material directions as purely linear elastic before damage initiation may therefore not only overestimate the local stiffness in matrix-dominated directions, but also alter the stress redistribution near the delamination front, thereby affecting the predicted onset of local sub-laminate buckling, intralaminar damage, and subsequent delamination growth. To address this issue, an intralaminar nonlinear progressive damage model was formulated by distinguishing the fiber- and matrix-dominated deformation mechanisms and was further coupled with an interlaminar cohesive zone model. The resulting framework provides a unified description of the compressive failure process of delaminated laminates, encompassing matrix nonlinear deformation, intralaminar damage accumulation, and interlaminar delamination propagation.

For the solid elements representing individual plies, the total strain is decomposed into elastic and plastic components as

$$\varepsilon = \varepsilon^{\mathrm{e}} + \varepsilon^{p} \tag{1}$$

where ε^{e} and ε^{p} denote the elastic and plastic strain tensors, respectively. Because the longitudinal response is predominantly carried by the high-stiffness fibers, plastic flow is restricted to the matrix-dominated transverse and shear directions to avoid non-physical plastic deformation along the fiber direction. Accordingly, the effective stress prior to damage degradation is expressed as

$$\sigma = C_0 : \left(\varepsilon - \varepsilon^{p} \right) \tag{2}$$

where C_0 is the undamaged orthotropic elastic stiffness tensor and $\tilde{\sigma}$ denotes the effective stress prior to stiffness degradation.

To describe the mechanical response in the matrix-dominated directions while ensuring rotational invariance of the plastic response about the fiber axis, the transversely isotropic plasticity model proposed by Vogler et al. [23] was adopted. Taking material direction 1 as the fiber direction, three stress invariants associated with matrix-dominated stress states are introduced as follows:

$$I_1 = \frac{1}{4}\left(\tilde{\sigma}_{22} - \tilde{\sigma}_{33}\right)^2 + \tilde{\tau}_{23}^2 \tag{3}$$

$$I_2 = \tilde{\tau}_{12}^2 + \tilde{\tau}_{13}^2 \tag{4}$$

$$I_3 = \tilde{\sigma}_{22} + \tilde{\sigma}_{33} \tag{5}$$

where I_1 represents the combined effect of the transverse normal stress difference and transverse shear stress on matrix yielding, I_2 characterizes the contribution of longitudinal shear, and I_3 represents the mean transverse normal stress state.

Based on the above stress invariants, the matrix yield function is expressed as:

$$F_p = \alpha_1 I_1 + \alpha_2 I_2 + \alpha_3 I_3 + \alpha_{32} I_3^2 - 1 \le 0 \tag{6}$$

Where $\alpha_1 = 1/\left(S_T^y\right)^2$, $\alpha_2 = 1/\left(S_L^y\right)^2$, S_T^y and S_L^y denote the transverse and longitudinal shear yield strengths, respectively, while the remaining coefficients are determined from the transverse uniaxial tensile, compressive, and biaxial transverse yield states. When $F_p < 0$, the material state remains within the current yield surface. Once the trial state reaches $F_p = 0$, the matrix enters the plastic regime, and the trial stress is corrected through a return-mapping algorithm.

After matrix yielding, the yield surface evolves with the accumulation of plastic deformation. Taking the accumulated equivalent plastic strain $\bar{\varepsilon}^p$ as the internal hardening variable, the yield strength for each characteristic loading mode is described by the following nonlinear hardening law:

$$Y_i^y = Y_{i0}^y + K_{h,i}\Phi\left(\bar{\varepsilon}^p, n_{h,i}\right) \tag{7}$$

where Y_{i0}^y denotes the initial yield strength for the i matrix-dominated loading mode, $K_{h,i}$ is the hardening amplitude parameter, $n_{h,i}$ controls the nonlinear evolution of the yield strength with accumulated plastic strain, and $\Phi(\cdot)$ denotes the corresponding hardening evolution function.

The plastic strain increment is determined from the plastic potential function G_p as:

$$d\varepsilon^p = d\lambda \frac{\partial G_p}{\partial \tilde{\sigma}} \tag{8}$$

where $d\lambda$ is the plastic multiplier. At each loading increment, an elastic predictor is first performed. If the trial stress lies outside the current yield surface, a plastic return-mapping procedure is employed to update the relevant plastic variables and hardening variables, yielding the plastically corrected effective stress.

After the matrix plastic correction, the current effective stress is used as the input for intralaminar damage evaluation. A three-dimensional Hashin criterion is employed to identify four failure modes, namely fiber tension, fiber compression, matrix tension, and matrix compression. Once any failure function reaches its critical value, the corresponding damage mode is activated. For matrix-dominated failure, damage initiation is evaluated using the effective stress obtained after the matrix plastic correction, thereby ensuring continuity between the pre-damage matrix nonlinear response and the subsequent damage initiation criterion.

The Hashin criterion is used only to identify damage initiation, while the subsequent stiffness degradation is described using a fracture-energy-based linear softening law. To reduce the mesh dependence associated with localized strain softening, the damage-driving equivalent strain ε_{eq} is converted into an equivalent displacement through the element characteristic length L_c:

$$\delta_r = L_c \varepsilon_{eq} \tag{9}$$

The energy dissipation from damage initiation to complete failure is further constrained by the critical fracture energy G_r^c associated with the corresponding failure mode:

$$G_r^c = \int_{\delta_r^0}^{\delta_r^f} \sigma_r d\delta_r \tag{10}$$

where δ_r^0 and δ_r^f denote the equivalent displacements at damage initiation and complete failure, respectively, for the i damage mode. As the equivalent displacement increases, the corresponding damage variable evolves continuously from 0 to 1, progressively reducing the effective stiffness associated with the affected material directions. This energy regularization ensures that the energy dissipated during intralaminar softening is consistent with the prescribed material fracture energy, thereby improving the robustness of progressive damage predictions with respect to variations in the local mesh size.

The interfacial behavior between adjacent plies is described using a bilinear cohesive zone model to represent the progressive delamination process of an initially intact interface, from elastic load transfer through damage initiation to complete failure. Prior to damage initiation, the interfacial tractions are related to the separation displacements through a linear traction–separation law:

$$t = K\delta \tag{11}$$

Where t denotes the interfacial traction vector, K is the initial interfacial stiffness matrix, and δ represents the normal and tangential separation displacements.

Interlaminar damage initiates when the normal and two tangential traction components satisfy the quadratic nominal stress criterion:

$$\left(\frac{\langle t_n \rangle}{t_n^0}\right)^2 + \left(\frac{t_s}{t_s^0}\right)^2 + \left(\frac{t_t}{t_t^0}\right)^2 = 1 \tag{12}$$

where $\langle \cdot \rangle$ denotes the Macaulay bracket, which is introduced to exclude the direct contribution of compressive normal traction to the initiation of opening-mode interfacial damage. After damage initiation, the cohesive stiffness progressively degrades with increasing effective separation, and the corresponding critical fracture energy is determined using the Benzeggagh–Kenane (B–K) mixed-mode fracture criterion.

Intralaminar progressive damage and interlaminar delamination are described using distinct constitutive formulations, while their mechanical coupling is achieved within the unified finite element solution through local deformation, stiffness degradation, and stress redistribution. The intralaminar material response is evaluated by the VUMAT at the integration points of the solid ply elements, sequentially performing the elastic predictor, matrix plasticity check and return mapping, Hashin damage evaluation, and fracture-energy-based damage variable update. The interlaminar interfaces are independently handled by cohesive elements according to the current traction–separation state to determine damage initiation and subsequent delamination growth. At the end of each time increment, both damage states contribute simultaneously to the update of the structural internal forces and the equilibrium solution of the subsequent increment.

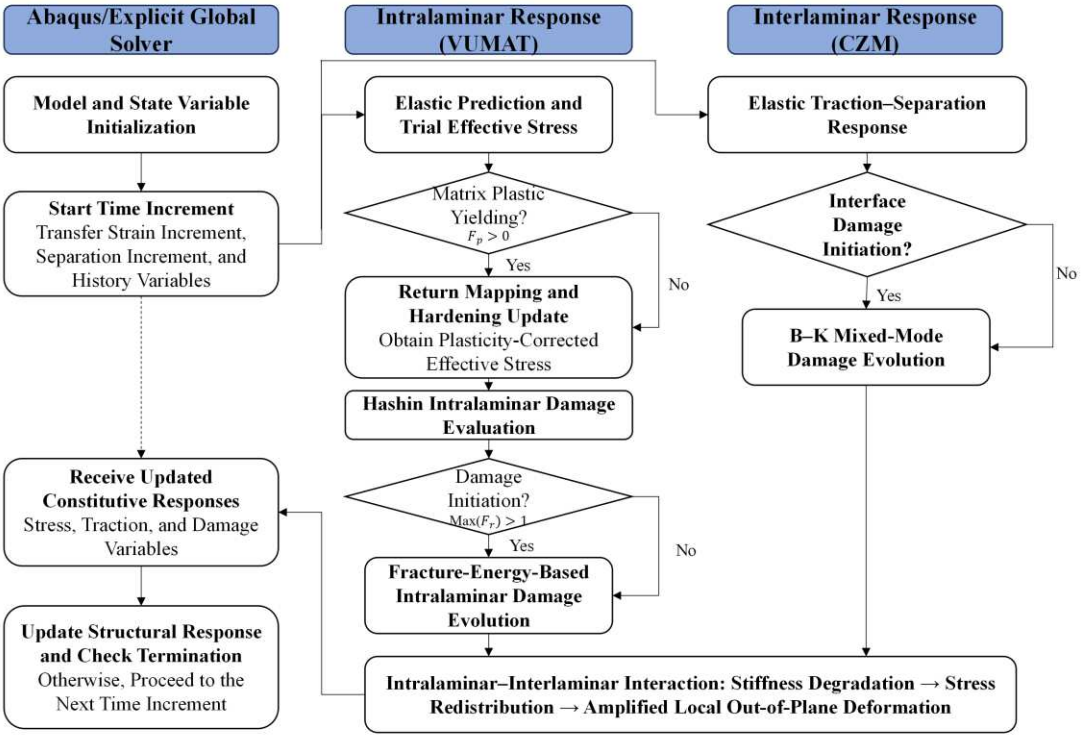


Fig. 1 Numerical implementation framework for coupled intralaminar-interlaminar damage and progressive failure

Figure 1 illustrates the numerical implementation of the coupled intralaminar–interlaminar damage framework. Within each explicit time increment, the global solver transfers the current strain increment, interface separation increment, and history variables to the material response update routines. For the solid ply elements, the update sequence consists of elastic prediction, matrix yielding assessment, return mapping, Hashin damage initiation, and fracture-energy-based stiffness degradation. For the cohesive interface elements, the traction–separation response is evaluated first, followed by interfacial damage initiation and mixed-mode delamination evolution governed by the B–K criterion. The initial delamination first reduces local stability and triggers out-of-plane deformation and sub-laminate buckling. The resulting stress redistribution then promotes both intralaminar and interlaminar damage, while the associated stiffness degradation further amplifies the local deformation. This interaction ultimately leads to a progressive compressive failure process characterized by the mutual enhancement of geometric instability and material damage.

2.2 Finite element model and delamination configurations

The spar cap is the primary longitudinal load-carrying component of a wind turbine blade and is predominantly reinforced with unidirectional fibers aligned along the blade span to sustain the axial tensile and compressive loads induced by bending. Under flapwise-bending in particular, the suction-side and pressure-side spar caps are subjected to significant axial compression and tension, respectively, making the local compressive stability and interlaminar integrity of the spar cap critical to the structural load-carrying performance of the blade. Previous studies on wind turbine spar structures have also shown that spar caps generally contain a high proportion of 0° unidirectional reinforcement to provide longitudinal stiffness and strength, while delamination can markedly alter local buckling and subsequent failure behavior [7]. In actual wind turbine blades, the spar exhibits spanwise variations in thickness, curvature, and cross-sectional geometry and forms a complex thin-walled load-carrying system together with the blade skins and shear webs. Direct use of a full-blade

model would introduce the simultaneous effects of cross-sectional variation, global bend–twist coupling, and complex load transfer, making it difficult to isolate the local effects of delamination size, through-thickness position, and multiple-delamination spatial configuration on local stability and damage evolution [26]. Therefore, a representative local laminate segment was extracted from the compressed spar-cap region and idealized as a constant-thickness rectangular laminate. While retaining the primary spanwise load-carrying direction, through-thickness ply arrangement, and interlaminar interface characteristics, uniaxial compression was employed to represent the local compressive state of the spar cap induced by blade bending.

2.2.1 Representative spar-cap laminate model and loading conditions

The $[0^o/90^o/0^o]_6$ layup adopted in this study is not intended to directly reproduce the stacking sequence of any specific commercial wind turbine blade spar cap. Instead, it represents a 0°-dominated laminate, with 0° plies accounting for 66.7% of the total ply count, so as to retain the fundamental longitudinal stiffness-dominated characteristics of the spar cap along the blade span. The laminate consists of 18 plies, each with a thickness of 0.138 mm, giving a total thickness of 2.484 mm. The overall model length and width are 180 mm and 20 mm, respectively, with 5 mm clamping regions applied at both ends, resulting in an effective loaded length L of 170 mm. A local material coordinate system was defined, with the X-direction aligned with the laminate longitudinal axis and primary loading direction, the Y-direction along the laminate width, and the Z-direction through the thickness.

To apply uniform axial compression, reference points were defined at both ends of the model, and the end-face nodes within the clamping regions were connected to the corresponding reference points through kinematic coupling constraints. At the fixed end, all translational and rotational degrees of freedom were constrained. At the loading end, the transverse and through-thickness translations, together with all rotational degrees of freedom, were restrained, while only the axial translational degree of freedom was retained. A displacement-controlled compressive load was then applied along the X-direction. The two longitudinal side edges were left unconstrained to avoid additional transverse restraints that could affect local out-of-plane buckling and post-buckling deformation in the delaminated region. The representative spar-cap laminate, stacking sequence, finite element model, and corresponding boundary and loading conditions are illustrated in Fig. 2.

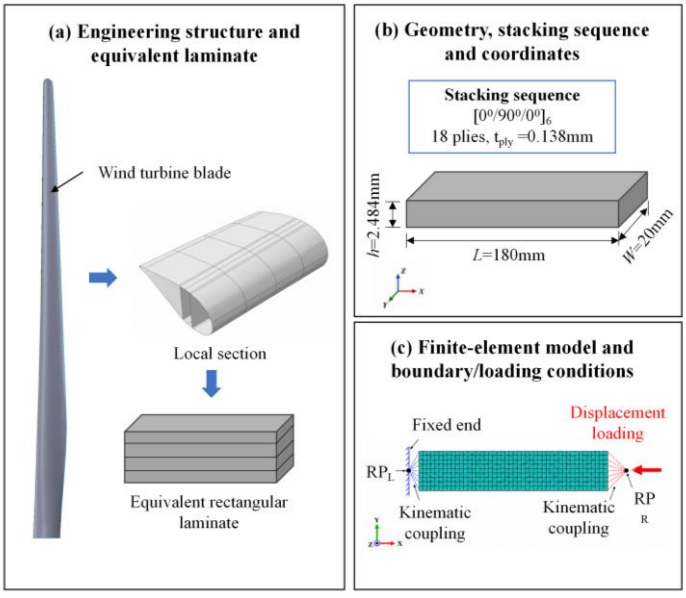


Fig. 2 Representative wind turbine blade spar-cap laminate and finite-element idealization

2.2.2 Finite element discretization and interface treatment

To simultaneously capture material anisotropy within individual plies, local out-of-plane buckling, and interlaminar delamination growth, each ply was discretized layer by layer using eight-node linear reduced-integration solid elements (C3D8R). The solid-element formulation allows distinct material orientations to be assigned to individual plies while retaining through-thickness stress components and local bending responses, thereby providing sufficient spatial resolution for the analysis of intralaminar damage, local sub-laminate buckling, and stress redistribution near the delamination front. The initially intact regions between adjacent plies were connected using eight-node three-dimensional cohesive elements (COH3D8), forming an alternating solid–cohesive interface–solid discretization scheme. For each delamination configuration, an eigenvalue buckling analysis was first performed, and the first buckling mode dominated by local out-of-plane deformation of the delaminated sub-laminate was selected as the initial geometric imperfection shape. Each mode was normalized with respect to its maximum out-of-plane displacement and uniformly scaled to ω_0=0.002 mm, ensuring a consistent imperfection amplitude among all delamination configurations. Quasi-static compression analyses were then conducted on the geometrically imperfect models to capture the complete evolution of local buckling, post-buckling deformation, and damage propagation.

The intralaminar constitutive response of the solid ply elements was implemented through the VUMAT described in Section 2.1, accounting for matrix-dominated elastic-plasticity, three-dimensional Hashin damage initiation, and fracture-energy-controlled intralaminar stiffness degradation. The initially intact interlaminar interfaces were modeled using a bilinear cohesive zone formulation to describe elastic load transfer, damage initiation, and delamination propagation under mixed-mode fracture.

For the initially delaminated regions, the corresponding interlaminar cohesive elements were removed in advance, and surface-to-surface contact was defined between the opposing delamination faces. Hard contact was adopted in the normal direction, allowing the delaminated surfaces to open freely during local buckling while preventing non-physical interpenetration when the surfaces closed under compression. In the tangential direction, the prescribed sliding formulation of the contact model was used. This treatment physically distinguishes the initial delamination from newly generated delamination caused by subsequent cohesive damage: the former is introduced as a predefined geometric defect, whereas the latter evolves according to the interfacial damage criterion and fracture-energy-based damage evolution law.

2.2.3 Delamination configuration design

To systematically investigate the effects of initial delamination geometry and spatial arrangement on the compressive response of laminated composites, four types of delamination configurations were considered while maintaining identical stacking sequence, material properties, boundary conditions, and loading conditions. These included single-delamination size, single-delamination through-thickness position, in-plane spacing between coplanar double delaminations, and through-thickness spacing between overlapping double delaminations, as illustrated in Fig. 3. The definitions of the corresponding parameters and the investigated cases are summarized in Table 1.

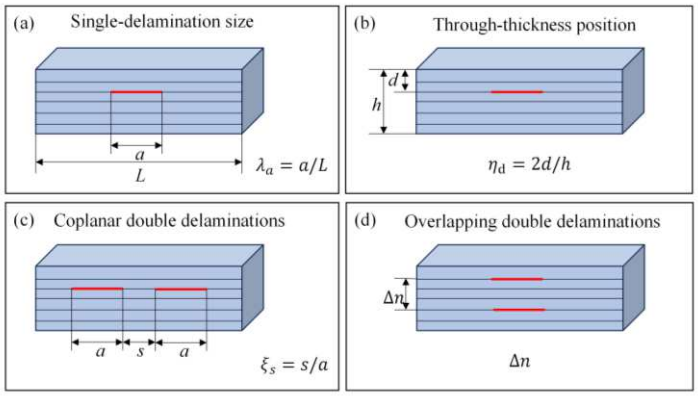


Fig. 3 Definition of the investigated delamination configurations

Table. 1 Definition of investigated delamination configurations

Configuration	Control parameter	Investigated values	Fixed conditions
Intact laminate	—	λ_a=0	—
Single delamination: size	$\lambda_a = a/L$	0.1-0.6	3rd/4th-ply interface
Single delamination: position	$\eta_d = 2d/h$	Corresponding interfaces	λ_a=0.3
Coplanar double delaminations	$\xi_s = s/a$	0, 0.5, 1.0, 1.5, 2.0	3rd/4th-ply interface
Overlapping double delaminations	Δn	3, 5, 7, 9, 11, 13	First delamination at 3rd/4th-ply

For the single-delamination size configurations, the ratio $\lambda_a = a/L$ of the delamination length a to the effective loaded length L of the laminate was adopted as the dimensionless size parameter. The delamination was located at the interface between plies 3rd and 4th and centered in-plane, with a/L=0, 0.1, 0.2, 0.3, 0.4, 0.5, and 0.6. Here, λ_a=0 represents the intact laminate without an initial delamination. For the through-thickness position configurations, λ_a was fixed at 0.3 and the in-plane delamination location was kept unchanged, while only the interlaminar position was varied. The through-thickness delamination position was characterized by η_d, where d denotes the distance from the delamination interface to the nearest outer surface and h is the total laminate thickness.

For the coplanar double-delamination configurations, both delaminations were located at the interface between plies 3rd and 4th, while the size of each individual delamination was kept constant. The relative in-plane spacing was characterized by the ratio $\xi_s = s/a$, where s denotes the clear distance between the adjacent delamination boundaries and a is the length of a single delamination. Values of ξ_s=0, 0.5, 1.0, 1.5, and 2.0 were considered, with ξ_s=0 indicating that the adjacent boundaries of the two delaminations were in contact. For the overlapping double-delamination configurations, the two delaminations had identical in-plane dimensions and coincident projected locations. The first delamination was fixed at the interface between plies 3rd and 4th, while only the interface location of the second delamination was varied. The through-thickness spacing was characterized by the number of plies Δn between the two delaminations, with Δn=3, 5, 7, 9, 11, and 13.

2.3 Parameter calibration, mesh convergence and model validation

To ensure a consistent numerical basis for the subsequent comparison of different delamination configurations, the finite element model was calibrated and validated from three aspects:

determination of material and interfacial parameters, spatial mesh discretization, and comparison with experimental data. The model parameters were determined by combining available experimental data with literature-based constraints, thereby avoiding indiscriminate adjustment of parameters associated with different physical mechanisms. Mesh discretization was assessed with respect to the convergence of the global compressive buckling response. Finally, published compression-test data were used to validate the model predictions of buckling initiation and the associated delamination-size effect in laminates containing initial delamination defects. This procedure provides a unified numerical basis for the subsequent parametric comparisons of post-buckling response, damage evolution, and load-carrying performance among different delamination configurations.

2.3.1 Parameter determination and calibration

The present model involves orthotropic elastic properties, intralaminar strength parameters, matrix elastic-plastic parameters, intralaminar damage-evolution parameters, and interlaminar interface parameters. Because these parameters govern different stages of the mechanical response and failure process, they were determined and calibrated separately rather than fitted simultaneously. The material data reported in Ref. [21] were used to determine the principal elastic constants, while the remaining three-dimensional elastic constants were obtained based on the assumption of transverse isotropy. The mechanical properties adopted for the composite laminate are summarized in Table 2.

Table. 2 Mechanical properties of the composite laminate

E_{11}	E_{22}	E_{33}	G_{12}	G_{13}	G_{23}
134GPa	10.2GPa	10.2GPa	5.52GPa	5.52GPa	5.52GPa
ν_{12}	ν_{13}	ν_{23}	X_T	X_C	ρ
0.3	0.3	0.3	850MPa	500MPa	1200kg/m^3

For the matrix-dominated transverse and shear nonlinear responses, the initial yield and hardening parameters were determined with reference to the three-dimensional transverse elastic-plastic damage model and the corresponding loading data reported by Goncalves et al. [25]. These parameters were further constrained using the pre-damage nonlinear stage of the laminate compressive response, so that the onset of plasticity and subsequent hardening remained consistent with the nonlinear deformation observed prior to damage initiation. The resulting matrix-dominated plasticity parameters are summarized in Table 3.

Table. 3 Parameters of the matrix-dominated plasticity model

Loading mode	Initial yield parameter, Y_{i0} (MPa)	Hardening parameter, $K_{h,i}$ (MPa)	Hardening exponent, $n_{h,i}$
Transverse uniaxial tension	60.85	34.90	0.2
Transverse uniaxial compression	197.60	348.70	0.2
Longitudinal shear	24.93	223.80	0.2
Transverse shear	40.20	221.20	0.2

The interlaminar interface parameters include the normal and tangential stiffnesses K_{nn}, K_{ss}, and K_{tt}, the interfacial strengths t_n^0, t_s^0, and t_t^0, the critical fracture energies for Modes I, II, and

III, G_{IC}, G_{IIC}, and G_{IIIC}, respectively, and the B–K exponent η. The initial values were determined based on relevant interlaminar fracture data and Ref. [8]. Among these parameters, the interface stiffness primarily governs the pre-damage interfacial deformation, the interfacial strengths control damage initiation, and the critical fracture energies determine the energy dissipation and softening evolution during delamination growth. Considering the relatively high sensitivity of the interface stiffness to local sub-laminate buckling and delamination initiation, it was calibrated within the physically reasonable range reported in the literature, while the remaining interface parameters were retained at their corresponding experimental values, as summarized in Table 4.

Table. 4 Interlaminar interface parameters of the composite laminate

K_{nn}	K_{ss}	K_{tt}	t_n^0	t_s^0
3.0×10^{14}N/mm^3	1.15×10^{14}N/mm^3	1.15×10^{14}N/mm^3	7.5MPa	15MPa
t_t^0	G_{IC}	G_{IIC}	G_{IIIC}	η
15MPa	200J/m^2	1000J/m^2	1000J/m^2	3.8

2.3.2 Mesh design and convergence assessment

For delamination growth modeled using cohesive elements, determining the mesh size solely from the global structural response is insufficient to ensure adequate spatial resolution of damage evolution near the crack front. A finite cohesive zone exists ahead of the delamination front, within which the interface progressively transitions from an intact state to complete failure, accompanied by pronounced spatial gradients in both traction and damage variables. Therefore, the local mesh size was first constrained based on the characteristic length of the cohesive zone. The cohesive-zone length can be generally expressed as:

$$L_{cz} = M\frac{E_{\mathrm{eff}}G_{\mathrm{c}}}{\left(\tau_0\right)^2} \tag{13}$$

where G_{c} is the critical fracture energy associated with the corresponding fracture mode, E_{eff} is the effective elastic modulus related to the crack-growth direction and material anisotropy, τ_0 is the interfacial strength, and M is a dimensionless coefficient associated with the cohesive-zone theory and the adopted interfacial constitutive formulation. For the orthotropic laminate considered in the present study, the expression can be further written, following the formulation adopted in the original model, as:

$$L_{cz} = \frac{E_{\mathrm{eff}}G_{\mathrm{c}}}{\left(\tau_0\right)^2} \tag{14}$$

To ensure that a sufficient number of elements are distributed within the cohesive zone to resolve the traction degradation and damage evolution, the local characteristic element size should satisfy the following condition when at least N_{cz} elements are required across the cohesive zone:

$$h_{cz} \le \frac{L_{cz}}{N_{cz}} \tag{15}$$

On this basis, a further mesh-convergence assessment was conducted for the global structural response. Taking the intact laminate without initial delamination as the reference case, the in-plane mesh size was varied while the stacking sequence, through-thickness discretization, material parameters, and boundary conditions were kept unchanged. Four mesh sizes, 1.2×1.2, 0.8×0.8,

0.5×0.5, and 0.3×0.3 mm^2, were considered. The buckling onset load N_{bk}, identified from the nonlinear compressive response, was adopted as the convergence indicator for the global structural response. The relative difference between two successive mesh levels was defined as:

$$e_i = \left| \frac{P_{bk}^{(i)} - P_{bk}^{(i-1)}}{P_{bk}^{(i-1)}} \right| \times 100\% \tag{16}$$

The buckling onset loads corresponding to the four mesh sizes were 3207.8, 3205.8, 3204.4, and 3203.7 N, respectively, as summarized in Table 5. As the mesh was refined from 1.2 mm to 0.3 mm, the total variation in the buckling onset load was only approximately 0.13%. In particular, further refinement from 0.5 mm to 0.3 mm resulted in a load difference of only 0.7 N, corresponding to a relative difference of 0.022%. These results indicate that the global compressive response had essentially reached mesh convergence.

Table. 5 Mesh convergence results for the buckling onset load

Element size (mm)	1.2×1.2	0.8×0.8	0.5×0.5	0.3×0.3
Buckling onset load, N_{bk} (N)	3207.8	3205.8	3204.4	3203.7
Relative difference between successive mesh level, η (%)	—	0.062	0.044	0.022

Considering both the convergence of the global structural response and the local spatial-resolution requirement of the cohesive zone, a nonuniform mesh was adopted for the subsequent delaminated models. An in-plane element size of approximately 0.5 mm was used away from the delaminated region, while the mesh was gradually refined to 0.3 mm near the delamination front and within the potential propagation region. This mesh scheme simultaneously satisfies the convergence requirement of the global buckling response and the local discretization requirement for resolving damage evolution near the delamination front, and was therefore applied consistently to all delamination configurations.

In addition, all subsequent nonlinear compression analyses employed the local sub-laminate buckling mode described in Section 2.2.2 as the initial geometric imperfection, with a consistent imperfection amplitude of ω_0=0.002 mm to avoid introducing additional differences among delamination configurations due to variations in the initial imperfection magnitude. Meanwhile, the axial displacement was applied using a Smooth Step amplitude in Abaqus/Explicit, and the total kinetic energy (ALLKE) and total internal energy (ALLIE) were continuously monitored throughout the analysis. Except for short-term energy fluctuations associated with local buckling or rapid delamination propagation, the ratio ALLKE/ALLIE remained below 5% during the simulations, indicating that significant inertial effects were effectively suppressed and that the explicit analyses satisfied the requirements for quasi-static loading.

2.3.3 Experimental validation of compressive buckling response

To evaluate the predictive capability of the developed numerical model for the compressive instability response of laminates containing initial delamination defects, the published compression-test results reported by Zhu et al. [21] were used for validation. Based on the specimen geometry, stacking sequence, delamination length, and through-thickness position reported in the original experiments, three finite element models, SD01, SD02, and SD03, were established with material properties, boundary conditions, and loading conditions consistent with the tests. The experiments showed that the delaminated specimens first underwent global buckling, while secondary buckling

in the locally delaminated region mainly developed during the post-buckling stage. Accordingly, a physical criterion consistent with the experiments was adopted in the present study: the buckling onset state was identified from the nonlinear compressive response as the point at which the global out-of-plane deformation began to develop noticeably, and the corresponding axial load was taken as the numerical buckling load for comparison with the experimental results.

The experimental and numerical results are summarized in Table 6. For specimens SD01, SD02, and SD03, with delamination lengths of 40, 80, and 120 mm, respectively, the experimentally measured mean buckling loads were 3100, 3000, and 2367 N, while the corresponding numerical predictions were 3388.9, 2924.3, and 2289.2 N. The relative errors were 9.32%, 2.52%, and 3.29%, respectively, giving a mean relative error of 5.04%. Both the experimental and numerical results exhibit the same trend of decreasing buckling load with increasing delamination length. The original experimental data reported by Zhu et al. likewise show a continuous reduction in buckling load as the delamination length increases from 40 to 120 mm.

Table. 6 Comparison between experimental and numerical buckling loads of delaminated laminates

Specimen	L (mm)	w (mm)	h (mm)	Delamination length, a(mm)	Numerical buckling load, (N)	Experimental buckling load, (N)	Relative error (%)
SD01	170	20	2.54	40	3388.9	3100	9.32%
SD02	170	20	2.60	80	2924.3	3000	2.52%
SD03	170	20	2.51	120	2289.2	2367	3.29%

These results demonstrate that the developed model can satisfactorily reproduce the onset of compressive buckling in laminates containing initial delamination defects, as well as its dependence on delamination size, thereby providing a consistent numerical basis for the subsequent comparative analyses of local stability, post-buckling deformation, and damage evolution under different delamination configurations. It should be noted that the present validation is focused primarily on the onset of compressive buckling, whereas the subsequent peak load-carrying state is jointly governed by post-buckling geometric nonlinearity, intralaminar damage, and interfacial degradation. Therefore, the ultimate load P_u and its normalized values used in the following sections are intended mainly for relative comparison of the degree of load-carrying degradation among different delamination configurations within the same numerical framework, rather than being interpreted directly as experimentally validated predictions of absolute ultimate strength.

3 Results and discussion

3.1 Delamination-induced compressive failure evolution

3.1.1 Global response and local deformation evolution

To clarify the influence of initial delamination on the global compressive response and the evolution of local instability, a representative case with a normalized delamination length of a/L=0.2 and the delamination located at the interface between plies 3rd and 4th was selected for analysis. The delamination locally separates the laminate through the thickness into a thinner and a thicker sub-laminate and removes the original interlaminar continuity constraint within the delaminated region. To characterize both the global load-carrying response and the local deformation, monitoring points U and L were defined on the upper and lower sub-laminate surfaces, respectively, at the projected center of the delaminated region, as shown in Fig. 4, and their out-of-plane displacements, U_3^U and U_3^L, were extracted. Figure 5 presents the axial load–displacement response together with the out-of-plane displacement histories of the two monitoring points, while Fig. 6 further shows the out-of-plane displacement fields corresponding to the characteristic states

A–D.

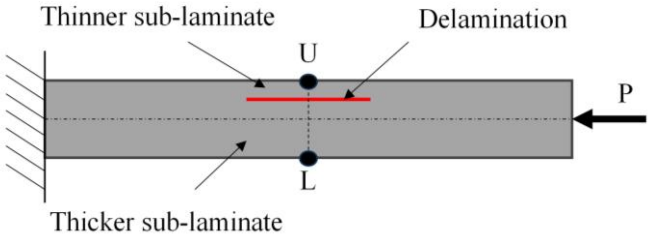


Fig. 4 Representative delaminated laminate and locations of monitoring points U and L

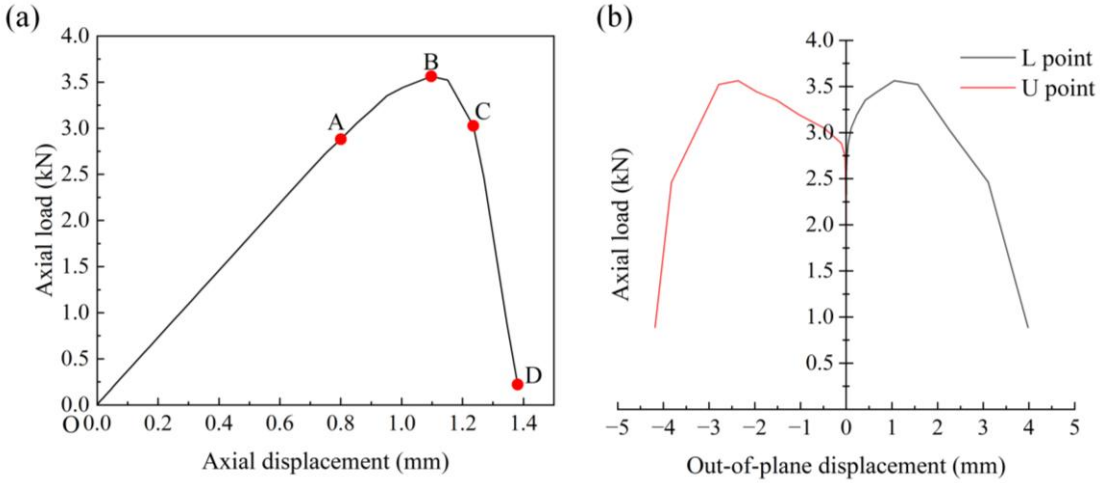


Fig. 5 Global and local responses of the representative delaminated laminate: (a) axial load-displacement response with characteristic states A-D; (b) Axial load versus out-of-plane displacements of monitoring points U and L

As shown in Fig. 5(a), the compressive response of the laminate containing an initial delamination can be divided into four characteristic stages: the stable compression stage O–A, the local sub-laminate buckling stage A–B, the post-buckling deformation stage B–C, and the global instability stage C–D. This stage division is primarily based on the evolution of the axial load–displacement response, together with the local out-of-plane displacement behavior shown in Fig. 5(b).

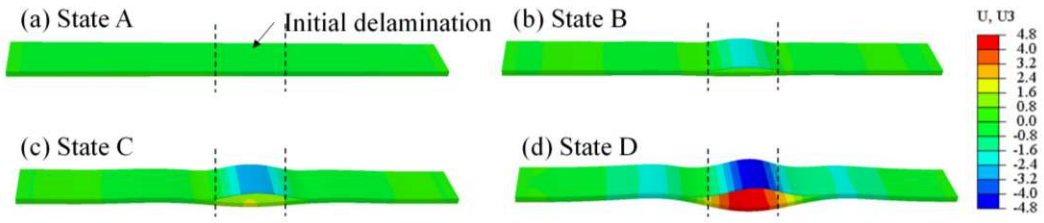


Fig. 6 Evolution of the out-of-plane displacement fields at characteristic loading states

During stage O–A, the axial load increases approximately linearly with displacement, while the out-of-plane displacements at both monitoring points remain small. As shown in Fig. 6(a), the laminate remains essentially flat, indicating that although the initial delamination disrupts the local through-thickness continuity, the surrounding intact laminate still provides sufficient constraint to suppress out-of-plane deformation within the delaminated region. Accordingly, this stage is dominated by global axial compression, and the influence of the initial delamination on the overall compressive stiffness remains relatively limited.

As the loading approaches point A, the response gradually enters stage A–B. As shown in Fig.

6(b), pronounced local out-of-plane deformation begins to develop within the delaminated region, with the thinner sub-laminate exhibiting a substantially larger deformation amplitude than the thicker sub-laminate. Meanwhile, the out-of-plane displacements at monitoring points U and L in Fig. 5(b) progressively diverge, indicating a transition from nearly compatible deformation of the two sub-laminates to distinctly asymmetric local bending. This behavior arises because the removal of the interlaminar constraint by the delamination produces different thicknesses and bending stiffnesses in the upper and lower sub-laminates, making the thinner sub-laminate more susceptible to local instability. Correspondingly, the axial load–displacement response begins to deviate from its initial linear path, accompanied by a gradual reduction in the global tangent stiffness.

After entering stage B–C, the structure has passed the local stability state near the peak load, while the out-of-plane deformation in the delaminated region continues to develop. As shown in Fig. 6(c), the extent of local bending further increases and the deformation incompatibility between the upper and lower sub-laminates becomes more pronounced. Meanwhile, the axial load-carrying level in Fig. 5(a) begins to decrease. These results indicate that the onset of local buckling does not immediately lead to global instability; instead, the laminate undergoes a distinct post-buckling deformation process. As the local bending deformation intensifies, the stress state near the delamination front becomes increasingly complex, thereby providing the mechanical conditions for subsequent interfacial degradation and delamination growth.

When the loading enters stage C–D, the amplitude of the out-of-plane deformation in Fig. 6(d) increases rapidly, while the locally deformed region expands into the surrounding laminate and gradually loses its localized character. At the same time, the axial load decreases sharply. At this stage, the structural response transitions from a post-buckling state dominated by local sub-laminate buckling to a more extensive instability mode, indicating that the remaining local stability is no longer sufficient to sustain the overall load-carrying capacity.

In summary, the compressive deformation of a representative delaminated laminate exhibits a continuous evolution from globally stable compression to local sub-laminate buckling, post-buckling deformation, and finally global instability. The initial delamination first alters the stability conditions of the separated sub-laminates by removing the local interlaminar constraint. Once local buckling develops, the progressively increasing out-of-plane deformation further modifies the local stress state near the delamination front. However, geometric deformation alone is insufficient to explain the rapid post-peak reduction in load-carrying capacity. It is therefore necessary to further examine the evolution of interfacial damage and newly generated delamination during the post-buckling process.

3.1.2 Interfacial damage evolution and delamination propagation

After local sub-laminate buckling develops, the out-of-plane deformation within the delaminated region continues to increase, accompanied by a reduction in the post-peak load-carrying level. To further clarify how this geometric instability evolves into interfacial degradation and newly generated delamination growth, the interfacial damage process at the characteristic states A–D is analyzed based on the spatial evolution of the cohesive-element damage variable SDEG shown in Fig. 7. The SDEG fields presented in Fig. 7 describe only the newly developed damage in the initially intact interfaces outside the predefined delaminated region. For the retained cohesive elements, SDEG=0 indicates that no interfacial stiffness degradation has occurred. As damage evolves, SDEG progressively increases from 0 to 1, corresponding to the transition of the interface from damage initiation to complete failure.

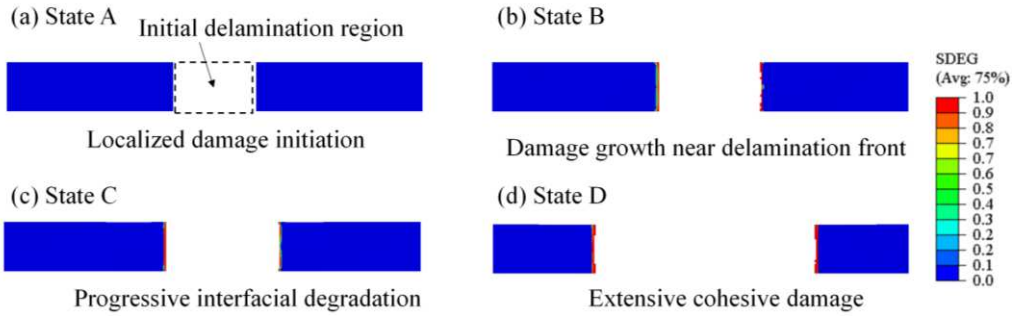


Fig. 7 Evolution of the interfacial damage variable SDEG at characteristic loading states

Near state A, most of the initially intact interface outside the predefined delamination front remains at a low SDEG level, indicating that no pronounced degradation of the interlaminar cohesive stiffness has yet occurred. At this stage, the initial delamination primarily alters the local stability conditions through the geometric discontinuity of the interface, without inducing significant newly generated interfacial damage. Therefore, the early-stage response is still governed mainly by changes in local structural stability.

As the response evolves from state A toward state B, local buckling of the thinner sub-laminate gradually develops, accompanied by the onset of localized SDEG growth near the delamination front, as shown in Fig. 7(b). The local bending deformation subjects the delamination front to more pronounced normal opening and tangential sliding, causing the adjacent initially intact cohesive elements to enter the damage-initiation stage first. At this stage, the damaged region remains largely confined to the vicinity of the initial delamination front and has not yet developed into widespread continuous degradation, indicating that stage A–B is still dominated by the formation of local buckling and the initiation of interfacial damage.

Once the response reaches the vicinity of state B and enters stage B–C, the high-SDEG region in Fig. 7(c) begins to propagate from the initial delamination front into the surrounding intact interface. As an increasing number of cohesive elements undergo stiffness degradation, a continuous region of newly generated interfacial damage progressively develops beyond the initial delamination, effectively enlarging the delaminated area. The resulting reduction in interfacial stiffness further weakens load transfer and constraint between the upper and lower sub-laminates. Therefore, during this stage, the interfacial damage evolves from localized initiation to progressive propagation and begins to exert a pronounced influence on the post-peak degradation of load-carrying capacity.

After entering stage C–D, the high-SDEG region in Fig. 7(d) expands further, and pronounced stiffness degradation develops over a larger portion of the initially intact interface, indicating continued propagation of newly generated delamination into the adjacent regions. As the effective continuity of interfacial load transfer progressively deteriorates, the original interlaminar constraint is further weakened, making it increasingly difficult to restrain the out-of-plane deformation of the sub-laminates within the delaminated region. Therefore, interfacial degradation is not merely a localized damage phenomenon near the delamination front, but a progressive process coupled with the overall instability evolution. Through continued loss of interfacial stiffness, it further weakens local constraint and promotes the development of out-of-plane deformation, ultimately leading to a reduction in compressive load-carrying capacity.

3.2 Single-delamination configuration effects

3.2.1 Effect of delamination size

Based on the single-delamination size configurations defined in Section 2.2.3, Fig. 8 presents

the axial load–displacement responses for different λ_a values, while Fig. 9 further compares the corresponding normalized ultimate load-carrying capacities. Because all cases employ identical stacking sequences, material properties, and boundary conditions, with delamination size being the only variable, the differences among the response curves can be directly attributed to the effect of delamination size on the compressive behavior.

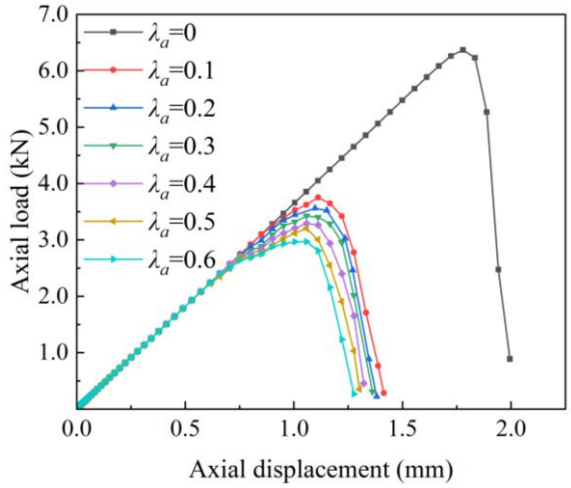


Fig. 8 Axial load-displacement response of laminates with different delamination sizes

As shown in Fig. 8, the different delamination-size cases exhibit similar axial responses during the initial loading stage, indicating that, before the onset of local instability, a finite-sized delamination has a relatively limited influence on the overall compressive deformation of the laminate. As the axial displacement increases, the load responses of the different cases gradually diverge. With increasing delamination size λ_a, the nonlinear transition occurs progressively earlier, while the peak load shows an overall decreasing trend. This indicates that increasing delamination size does not directly cause a pronounced change in the initial global compressive stiffness; instead, it alters the local stability conditions within the delaminated region, reduces the resistance of the sub-laminate to out-of-plane deformation, and thereby promotes earlier local instability.

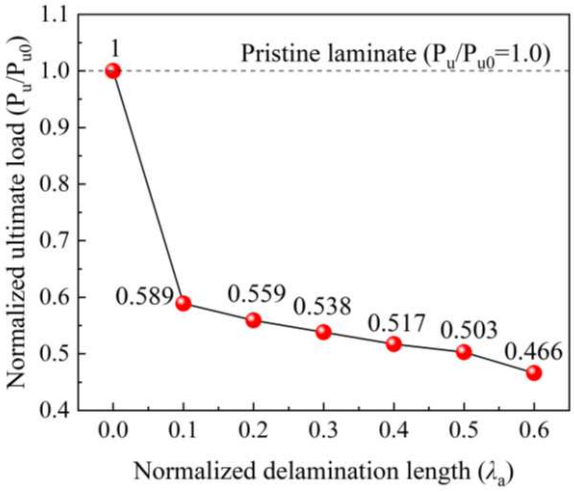


Fig. 9 Effect of delamination size on the normalized ultimate load-carrying capacity

From the perspective of local stability, when the delamination position and stacking sequence remain unchanged, increasing λ_a primarily increases the effective unsupported length of the delaminated sub-laminate. As a result, the local response gradually shifts from being governed by the constraint of the intact laminate to being dominated by the bending stiffness of the separated

sub-laminate itself. According to local buckling theory, the critical stability capacity of the sub-laminate is strongly dependent on its effective unsupported length; therefore, increasing the delamination size reduces the critical load required to trigger local buckling. This is reflected in the axial load–displacement response by an earlier onset of nonlinearity, a lower peak load-carrying capacity, and more pronounced post-peak degradation.

Figure 9 further presents the normalized variation in ultimate load-carrying capacity for different delamination sizes λ_a. Taking the ultimate load of the intact laminate, P_{u0}, as the reference, the normalized ultimate load $\bar{P}_u = P_u/P_{u0}$ decreases continuously with increasing delamination size, indicating a progressive reduction in compressive load-carrying capacity as the delaminated region enlarges. When the delamination is relatively small, the delaminated region remains constrained by the surrounding intact plies and adjacent interfaces, which limits the development of local instability and results in a comparatively gradual reduction in ultimate capacity. As λ_a increases further, the effective unsupported length of the delaminated sub-laminate increases, causing local buckling to occur earlier and inducing more pronounced bending deformation and interlaminar stress concentration near the delamination front. These effects promote interfacial damage propagation and further reduce the structural load-carrying capacity. Therefore, the reduction in ultimate load-carrying capacity with increasing delamination size cannot be attributed simply to the increase in defect area. More fundamentally, the delamination size modifies the local stability conditions. As the effective unsupported region expands, the delaminated sub-laminate becomes increasingly susceptible to local instability, while the associated secondary bending and interfacial degradation further weaken the overall structural stability. Consequently, the compressive failure mechanism gradually evolves from one dominated primarily by the presence of a local defect to one governed by the coupled effects of local buckling and progressive damage.

Overall, the influence of delamination size on the compressive performance of the laminate is governed primarily by the reduction in local stability. Small delaminations mainly weaken the local interlaminar constraint, whereas larger delaminations enlarge the effective unsupported region, promote earlier local buckling, and subsequently accelerate interfacial degradation and the reduction in ultimate load-carrying capacity. Therefore, for a single delamination at a fixed through-thickness position, the effective unsupported length represents an important mechanical parameter linking delamination geometry to the degradation of compressive load-carrying capacity.

3.2.2 Effect of through-thickness delamination position

With the delamination size held constant, the through-thickness position determines the thickness combination of the upper and lower sub-laminates formed by the delamination. Based on the through-thickness position cases defined in Section 2.2.3, Figs. 10 and 11 present the axial load–displacement responses and the corresponding normalized ultimate load-carrying capacities for different η_d values, respectively.

As shown in Fig. 10, with the delamination size held constant, the axial compressive responses differ noticeably with through-thickness delamination position. The initial portions of the axial load–displacement curves are generally similar among the different cases, indicating that the delamination position has only a limited influence on the initial global compressive stiffness before the onset of local instability. As loading proceeds, the responses begin to diverge. Delaminations located near the laminate surface exhibit an earlier onset of nonlinearity and relatively lower peak loads, whereas moving the delamination toward the laminate mid-plane shifts the nonlinear stage to a later loading level and allows the structure to sustain a higher axial load. These numerical results indicate that the through-thickness position of the delamination does not significantly alter the initial global stiffness, but plays an important role in governing the local stability of the separated sub-

laminates.

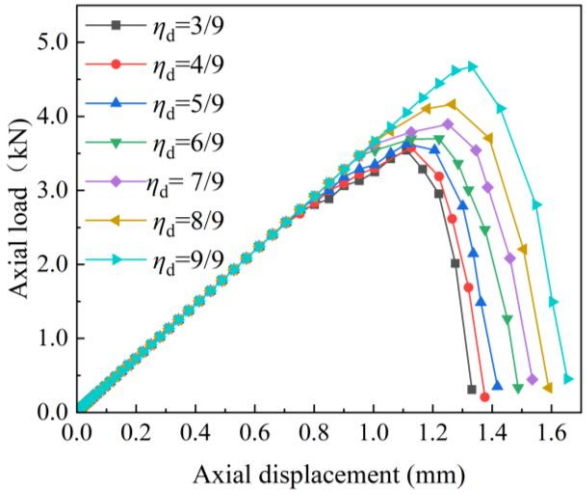


Fig. 10 Axial load-displacement responses of laminates with different through-thickness delamination positions

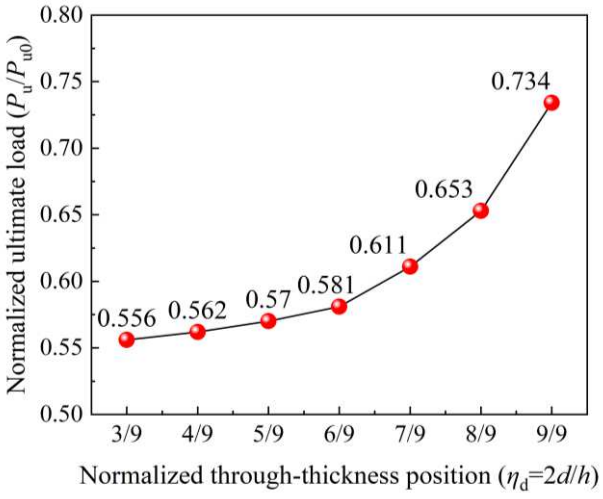


Fig. 11 Effect of through-thickness delamination position on the normalized ultimate load-carrying capacity

For delaminations with the same in-plane dimensions but located at different interfaces, the resulting upper and lower sub-laminates have different thickness combinations. A near-surface delamination produces a relatively thin outer sub-laminate with lower bending stiffness, making it more susceptible to local buckling under axial compression. Once local out-of-plane deformation develops, the associated secondary bending and interlaminar interactions near the delamination front become more pronounced, causing the structural response to depart from the stable compression path at an earlier stage. As the delamination moves toward the geometric mid-plane, the thicknesses of the two sub-laminates become more balanced, and the thinner sub-laminate becomes thicker. Its resistance to local out-of-plane bending therefore increases, suppressing local instability and improving the peak load-carrying capacity.

Figure 11 further presents the normalized variation in ultimate load-carrying capacity for different through-thickness delamination positions. Taking the ultimate load of the intact laminate, P_{u0}, as the reference, the normalized ultimate load is defined as $\bar{P}_u = P_u/P_{u0}$. As the delamination moves from the near-surface region toward the laminate mid-thickness, the normalized ultimate load shows an overall increasing trend. This indicates that, within the range of through-thickness positions investigated in the present study, near-surface delaminations cause a more pronounced

degradation in compressive load-carrying capacity, whereas delaminations located closer to the laminate mid-plane have a relatively weaker effect on the ultimate load-carrying capacity.

The effect of through-thickness delamination position should not be interpreted simply as a case in which a delamination closer to the surface is inherently more detrimental. Rather, the delamination position modifies the thickness and bending-stiffness distribution of the separated sub-laminates. For a laminate sub-laminate, the out-of-plane bending stiffness exhibits a strong dependence on thickness and may be expressed conceptually as $D \propto h_s^3$, where h_s denotes the thickness of the corresponding sub-laminate. Therefore, when the delamination is located near the outer surface, the thinner sub-laminate has a substantially lower bending stiffness and hence a lower critical level for local buckling. As the delamination moves toward the laminate mid-plane, the thickness of the thinner sub-laminate increases, the stiffness mismatch between the upper and lower sub-laminates is reduced, and a higher load is required to trigger local buckling. Consequently, the structure is able to sustain a higher ultimate load-carrying capacity.

Overall, for a fixed delamination size, the through-thickness position primarily governs the local stability by altering the thickness combination and bending-stiffness distribution of the upper and lower sub-laminates. A near-surface delamination produces a thin sub-laminate with low bending stiffness, promoting earlier local buckling and a more pronounced reduction in ultimate load-carrying capacity. As the delamination moves toward the laminate mid-thickness, the stiffness distribution of the separated sub-laminates becomes more balanced, local stability is improved, and the ultimate load-carrying capacity correspondingly recovers. Therefore, the effect of through-thickness delamination position is governed mainly by its influence on sub-laminate thickness and bending-stiffness distribution.

3.3 Effects of multiple-delamination spatial configurations

3.3.1 Effect of in-plane spacing between coplanar double delaminations

In practical laminated structures, delamination defects may coexist as multiple discrete regions. Their compressive response is governed not only by the geometric characteristics of individual defects, but also by the spatial relationships among them. For coplanar double delaminations located at the same interface, the width of the intact material ligament between the two defects may alter the local constraint and load-transfer conditions of the delaminated regions. Based on the coplanar double-delamination cases defined in Section 2.2.3, Figs. 12 and 13 present the axial load–displacement responses and the corresponding normalized ultimate load-carrying capacities for different relative in-plane spacings ξ_s, respectively.

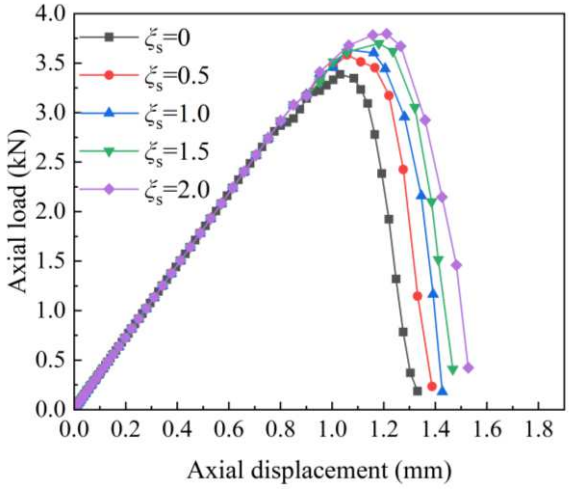


Fig.12 Axial load-displacement responses of laminates with different coplanar double delamination spacings

As shown in Fig. 12, the axial load–displacement curves for the different spacing cases nearly coincide during the initial loading stage, indicating that the in-plane spacing between the two delaminations has only a limited influence on the initial global compressive stiffness before a pronounced nonlinear response develops. As the axial displacement increases, the curves gradually diverge. With increasing s/a, the nonlinear transition and peak response shift toward higher load levels and larger axial displacements, accompanied by a progressive increase in peak load. This indicates that varying the spacing between the two delaminations primarily affects local stability and the ultimate load-carrying stage, rather than significantly altering the initial global axial stiffness. When s/a=0, the boundaries of the two delaminations are adjacent, and the two defects, each of length a, form a relatively large continuous region with reduced interlaminar constraint. In this configuration, no intact interfacial ligament exists between the two delaminations to provide additional local constraint to the separated sub-laminates, resulting in a larger effective unsupported region and, consequently, the lowest ultimate load-carrying capacity among the investigated cases. As s/a increases, the intact material ligament between the two delaminations becomes wider and progressively contributes to local deformation restraint and load transfer. The two delaminations therefore behave less like a single continuous long defect, leading to a gradual recovery of the ultimate load-carrying capacity.

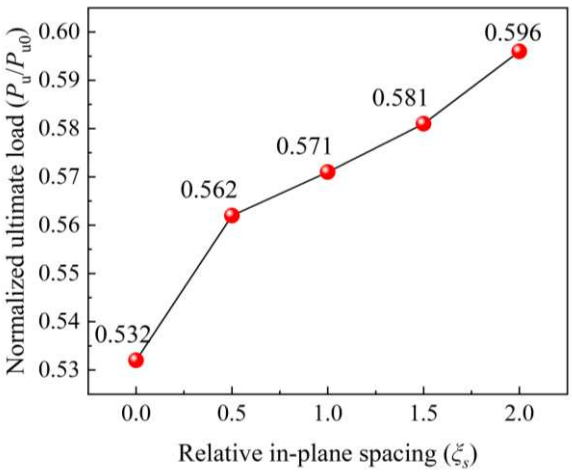


Fig. 13 Effect of coplanar double-delamination spacing on the normalized ultimate load-carrying capacity

Figure 13 further quantifies the effect of in-plane spacing on the ultimate load-carrying capacity. Taking the ultimate load of the intact laminate, P_{u0}, as the reference, the normalized ultimate load P_u/P_{u0} increases from 0.532 to 0.562, 0.571, 0.581, and 0.596 as s/a increases from 0 to 2.0, exhibiting a continuous recovery trend. From s/a=0 to 2.0, the normalized ultimate load increases by 0.064, corresponding to an improvement of approximately 12.0% relative to the s/a=0 case. This indicates that the in-plane separation distance between the two delaminations has a non-negligible influence on the residual compressive load-carrying capacity.

A closer comparison of the individual spacing intervals shows that, as s/a increases from 0 to 0.5, the normalized ultimate load rises from 0.532 to 0.562, indicating a relatively pronounced recovery. With further increases in spacing, the load-carrying capacity continues to improve, although at a more gradual rate. This suggests that the most evident improvement in local stability occurs when the two delaminations transition from directly adjacent boundaries to a configuration separated by a finite intact material ligament. Further widening of this intact region continues to enhance the structural load-carrying capacity, but with a progressively reduced rate of recovery.

Overall, the in-plane spacing between coplanar double delaminations affects the compressive load-carrying performance primarily by altering the width of the intact material ligament between

the two defects and the corresponding local constraint conditions. When s/a=0, the adjacent delaminations form a relatively large continuous region with reduced interlaminar constraint, which is most unfavorable to local stability. As the in-plane spacing increases, the constraint and load-transfer functions of the intact material between the two delaminations are progressively restored, leading to a corresponding increase in the ultimate load-carrying capacity. Therefore, within the parameter range investigated in this study, coplanar double delaminations exhibit a progressive recovery in load-carrying response with increasing in-plane spacing.

3.3.2 Effect of through-thickness spacing between overlapping double delaminations

Unlike coplanar double delaminations, which primarily modify the width of the intact in-plane material ligament, overlapping double delaminations with coincident in-plane projections form a local through-thickness configuration consisting of multiple sub-laminates. Their compressive response is therefore additionally influenced by the thickness and stiffness distribution of the intermediate sub-laminate. Based on the overlapping-delamination cases defined in Section 2.2.3, Figs. 14 and 15 present the axial load–displacement responses and the corresponding normalized ultimate load-carrying capacities for different through-thickness spacings Δn, respectively.

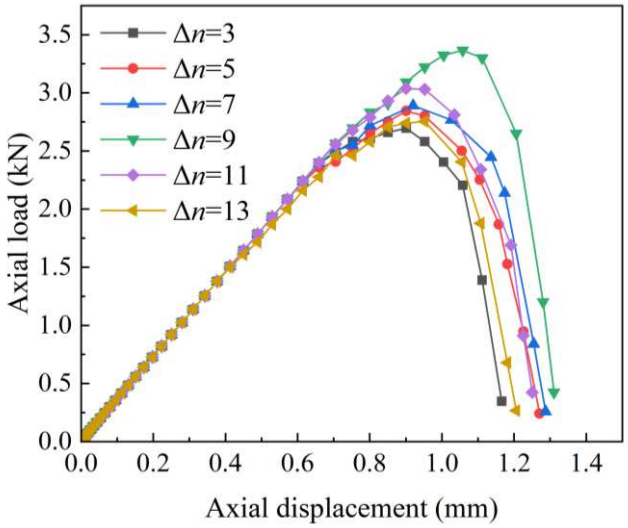


Fig. 14 Axial load-displacement responses of laminates with different through-thickness spacings between overlapping double delaminations

As shown in Fig. 14, all through-thickness spacing cases exhibit an approximately linear increase during the initial loading stage, indicating that the initial axial compressive stiffness is governed primarily by the intact laminate structure, while the through-thickness configuration of the double delaminations has only a limited influence on the initial elastic response. As the loading enters the nonlinear regime, the responses of the different spacing cases begin to diverge, and both the peak load and the post-peak degradation exhibit a pronounced non-monotonic dependence on the through-thickness spacing.

As Δn increases from 3 to 5, the peak load of the load–displacement response increases. With increasing through-thickness spacing, the intermediate sub-laminate becomes thicker, resulting in an increase in its bending stiffness and local load-transfer capability. This, in turn, improves the local stability of the overlapping-delamination region and allows a partial recovery of the local load-carrying capacity. These results indicate that the effect of through-thickness spacing is not governed by geometric separation alone, but depends on how the thickness and stiffness configuration of the intermediate sub-laminate modifies the local stability state.

As Δn further increases to 7 and 9, the intermediate sub-laminate becomes progressively thicker, enhancing its capacity for independent deformation while still maintaining relatively strong mechanical interaction with the upper and lower delaminated regions. This behavior can be interpreted as a consequence of the redistribution of local bending stiffness associated with the increased thickness of the intermediate sub-laminate, which improves the stability conditions within the overlapping-delamination region. Consequently, the Δn=9 case exhibits the highest ultimate load-carrying capacity. According to Fig. 15, its normalized ultimate load reaches approximately 0.528, representing the maximum value among all investigated overlapping double-delamination configurations.

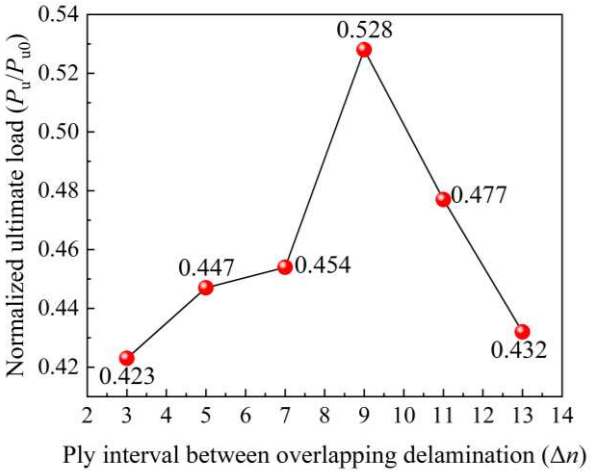


Fig.15 Effect of through-thickness spacing on the normalized ultimate load-carrying capacity of laminates with overlapping delaminations

Figure 15 further reveals the influence of through-thickness spacing on the ultimate load-carrying capacity. As Δn increases from 3 to 9, the normalized ultimate load gradually rises from 0.423 to 0.528, corresponding to an increase of approximately 24.8%. This trend indicates that increasing the through-thickness spacing between the two delaminations can improve the local sub-laminate stiffness configuration and create a more effective mechanical buffer region between the two delaminated zones. However, when Δn is further increased to 11 and 13, the normalized ultimate load decreases to 0.477 and 0.432, respectively, exhibiting a distinct recovery-then-degradation trend. This behavior can be attributed to the fact that, although a larger separation between the two delaminations reduces their direct interaction, the upper and lower delaminations progressively behave as relatively independent local defect regions. Under these conditions, the overall load-carrying capacity becomes increasingly governed by the local stability of the two individual delaminated regions, and the beneficial stiffness coordination provided by the intermediate sub-laminate can no longer produce further improvement in structural capacity.

Therefore, the through-thickness spacing of overlapping double delaminations exhibits a distinct configuration effect. On the one hand, when the spacing is small, the intermediate sub-laminate is relatively thin and the two delaminated regions remain strongly coupled in deformation, which is unfavorable to local stability. On the other hand, an intermediate through-thickness spacing allows the formation of an intermediate sub-laminate with sufficient load-carrying capability, enabling more effective stiffness coordination between the two defect regions and thereby improving local structural stability. When the spacing is increased further, the responses of the two delaminations become progressively more independent, and the local defect effects again become

dominant, resulting in a reduction in load-carrying capacity.

Overall, the through-thickness configuration effect of overlapping double delaminations is not governed solely by the geometric separation between the two defects, but by the redistribution of bending stiffness caused by changes in the intermediate sub-laminate thickness and by the deformation compatibility between the delaminated regions. Within the range investigated in this study, the configuration with Δn=9 exhibits a relatively high ultimate load-carrying capacity, whereas both smaller and larger through-thickness spacings lead to reduced structural load-carrying performance.

3.4 Mechanistic synthesis of configuration-dependent load-carrying degradation

The preceding results demonstrate that all investigated delamination configurations reduce the compressive load-carrying capacity of the laminate, although the underlying degradation pathways are not identical. Single delaminations primarily govern the structural response by altering the local stability conditions of the separated sub-laminates, whereas multiple delaminations are additionally influenced by the spatial arrangement of the defects and the associated local stiffness configuration. It is therefore necessary to summarize the intrinsic mechanisms governing delamination-induced compressive degradation from a unified mechanical perspective.

For a single delamination, the delamination size and through-thickness position affect local stability by altering the effective unsupported length and the bending-stiffness distribution of the separated sub-laminates, respectively. An increase in delamination size enlarges the region over which the sub-laminate can deform freely, making local out-of-plane buckling more likely. In contrast, variation in the through-thickness position changes the thickness ratio of the upper and lower sub-laminates, resulting in different bending-stability capacities among the various configurations. Therefore, under single-delamination conditions, the degradation in load-carrying capacity fundamentally originates from the reduction in local stability.

For multiple delaminations, the structural response is further governed by the spatial configuration of the individual defect regions. For coplanar double delaminations, the in-plane spacing determines the constraining effect of the intact material ligament between the defects, and increasing the spacing improves the local stability conditions. For overlapping double delaminations, the through-thickness spacing alters the thickness and stiffness distribution of the intermediate sub-laminate, resulting in a pronounced non-monotonic load-carrying response. Therefore, the effect of multiple delaminations is not governed simply by an increase in the number of defects, but by the local structural configuration formed by the spatial arrangement of the individual delaminated regions.

A synthesis of the responses associated with the different delamination configurations shows that, although delamination size, through-thickness position, and multiple-delamination spatial arrangement produce different trends in load-carrying performance, their effects ultimately converge on changes in the local constraint state and sub-laminate stiffness distribution. For a single delamination, the delamination size primarily governs the effective unsupported extent of the delaminated region, whereas the through-thickness position determines the thickness and bending-stiffness configuration of the upper and lower sub-laminates. For multiple delaminations, the in-plane spacing between coplanar delaminations modifies the constraining effect of the intact material ligament between the defects, while the through-thickness spacing between overlapping delaminations further regulates the thickness and stiffness configuration of the intermediate sub-laminate. Accordingly, the influence of different delamination configurations on compressive load-carrying performance can be summarized as a continuous mechanical process of configuration change → alteration of local stability → damage evolution → reduction in local effective load-

transfer capability, as schematically illustrated in Fig. 16.

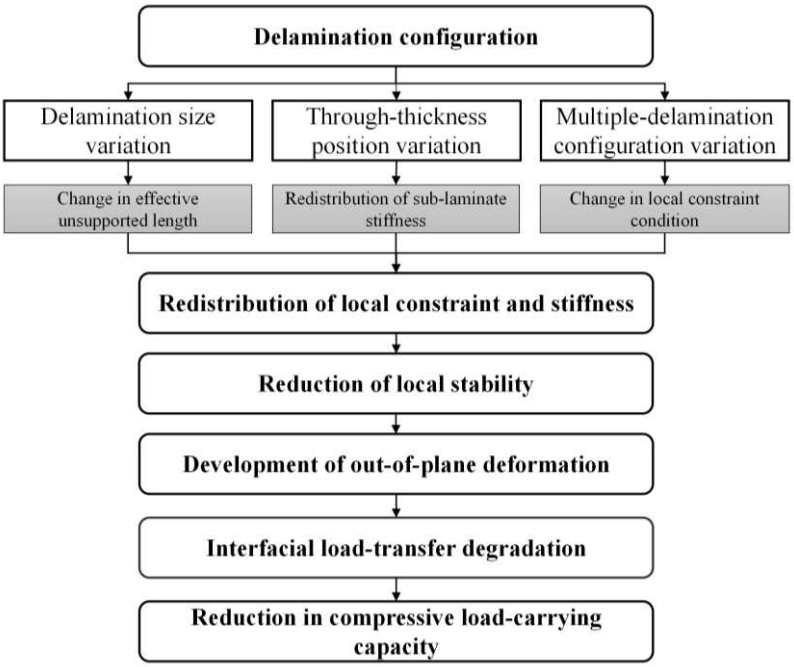


Fig. 16 Schematic illustration of the configuration-dependent compressive degradation mechanism of delaminated laminates

As illustrated in Fig. 16, different delamination configurations first modify the effective unsupported extent, the sub-laminate stiffness configuration, and the constraint relationships among neighboring defects, thereby reconstructing the local constraint conditions and stiffness distribution within the delaminated region. Under axial compression, these changes in local structural characteristics reduce the stability of the sub-laminates and make the delaminated region more susceptible to out-of-plane deformation. As local buckling develops, secondary bending and interlaminar stress concentrations near the delamination front become progressively more pronounced, further driving the initiation and propagation of interfacial damage. The resulting interfacial stiffness degradation, in turn, weakens the original interlaminar constraint and the continuity of local load transfer, progressively reducing the effective load-transfer paths and ultimately leading to a decrease in the ultimate load-carrying capacity. Therefore, the delamination configuration does not directly determine the macroscopic ultimate load. Rather, its effect is exerted by reconstructing the local stability boundary conditions and thereby governing the subsequent failure evolution. The differences in load-carrying response among the various delamination configurations can thus be understood within a unified framework in terms of the combined effects of effective unsupported length, sub-laminate bending stiffness, and spatial constraint relationships among multiple defects.

4 Conclusions

This study investigated delamination-induced compressive failure in representative wind turbine blade spar-cap laminates using a three-dimensional finite element framework incorporating matrix-dominated nonlinearity, intralaminar progressive damage, and interlaminar delamination growth. The main conclusions are as follows.

(1) Initial delamination induces a progressive compressive failure process governed by local sub-laminate instability. The defect first weakens the local interlaminar constraint with limited influence on the initial axial stiffness. With increasing compression, local buckling develops in the

thinner sub-laminate, followed by interfacial damage propagation and further loss of load-transfer continuity, ultimately leading to rapid degradation of the post-buckling load-carrying capacity.

(2) Delamination size primarily affects compressive performance by changing the effective unsupported length of the sub-laminate. Increasing the normalized delamination length advances the nonlinear transition and peak state and continuously reduces the ultimate load-carrying capacity. At a/L=0.6, the ultimate load is approximately 53% lower than that of the intact laminate, indicating that the size effect is mainly controlled by local stability rather than defect area alone.

(3) The through-thickness position of a delamination controls local stability through the thickness and bending-stiffness distribution of the separated sub-laminates. Near-surface delamination produces a thinner and less stable outer sub-laminate, whereas moving the defect toward the laminate mid-thickness improves stiffness balance and local stability. Accordingly, the normalized ultimate load increases from approximately 0.556 to 0.734 over the investigated positions.

(4) The in-plane spacing between coplanar double delaminations governs the interaction between adjacent defect regions through the intact material ligament. Increasing the spacing restores local constraint and load-transfer capability, resulting in a continuous increase in the normalized ultimate load from 0.532 to 0.596, corresponding to an improvement of about 12%. Thus, the response of coplanar double delaminations cannot be represented by a simple superposition of two isolated defects.

(5) Overlapping double delaminations exhibit a distinct non-monotonic through-thickness spacing effect. As the spacing increases from Δn=3 to 9, the normalized ultimate load rises from 0.423 to 0.528, whereas further increases to Δn=11 and 13 reduce it to 0.477 and 0.432, respectively. This behavior results from the combined effects of intermediate sub-laminate thickness, bending-stiffness redistribution, and mechanical interaction between the delaminated regions.

Overall, the effects of different delamination configurations can be unified in terms of changes in effective unsupported length, sub-laminate stiffness distribution, and local constraint conditions, which jointly govern local instability, interfacial damage propagation, and compressive load-carrying degradation. Delamination assessment should therefore consider not only defect size and number, but also through-thickness position and spatial configuration. Future work should extend the present framework to more realistic spar-cap geometries and fatigue loading conditions.

CRediT authorship contribution statement

Wenhu Gu: Conceptualization, Methodology, Writing – original draft. **Xin Cai**: Supervision, Writing – review & editing. **Qinhui Liu**: Formal analysis. **Min Li**: Data curation, Software, Validation. **Yanan Zhang**: Visualization.

Declaration of Competing Interest

The authors declare that they have no known competing financial interests or personal relationships that could have appeared to influence the work reported in this paper.

Acknowledgement

The authors are grateful to the Open Fund of Jiangsu Wind Power Engineering Technology Center of China (No. ZK22-03-05), and the Key Laboratory of Ministry of Education for Coastal Disaster and Protection (No. 202207).

References

1. Liu, Y., Li, N., Wang, P., Wang, T., Zhou, J., Qin, Z., Chu, F.: A review of vibration analysis and suppression for wind turbine blades: State of the art, challenges and perspectives. Thin-Walled Struct. 218, 114095 (2026). https://doi.org/10.1016/j.tws.2025.114095

971 2. Sun, S., Wang, T., Chu, F.: In-situ condition monitoring of wind turbine blades: A critical and
972 systematic review of techniques, challenges, and futures. Renew. Sustain. Energy Rev. 160, 112326
973 (2022). https://doi.org/10.1016/j.rser.2022.112326
974 3. Martulli, L.M., Diani, M., Sabetta, G., Bontumasi, S., Colledani, M., Bernasconi, A.: Critical review
975 of current wind turbine blades' design and materials and their influence on the end-of-life
976 management of wind turbines. Eng. Struct. 327, 119625 (2025).
977 https://doi.org/10.1016/j.engstruct.2025.119625
978 4. Haselbach, P.U., Berring, P.: Spar cap/shear web debonding under fatigue loading studied on the DTU
979 12.6 m wind turbine blade. Procedia Struct. Integr. 57, 169–178 (2024).
980 https://doi.org/10.1016/j.prostr.2024.03.020
981 5. Gohar, I., Yew, W.K., Halimi, A., See, J.: Review of state-of-the-art surface defect detection on wind
982 turbine blades through aerial imagery: Challenges and recommendations. Eng. Appl. Artif. Intell.
983 144, 109970 (2025). https://doi.org/10.1016/j.engappai.2024.109970
984 6. Tan, W., Naya, F., Yang, L., Chang, T., Falzon, B.G., Zhan, L., Molina-Aldareguía, J.M., González, C.,
985 Llorca, J.: The role of interfacial properties on the intralaminar and interlaminar damage behaviour
986 of unidirectional composite laminates: Experimental characterization and multiscale modelling.
987 Compos. Part B Eng. 138, 206–221 (2018). https://doi.org/10.1016/j.compositesb.2017.11.043
988 7. Li, H., Ning, W., Xin, W., Xu, B.: Study on the delamination damage prediction of wind turbine blade
989 spar cap based on morphology feature recognition. Eng. Fail. Anal. 166, 108867 (2024).
990 https://doi.org/10.1016/j.engfailanal.2024.108867
991 8. Li, H., Xin, W., Xu, B., Bao, H.: Delamination failure analysis of wind turbine blades based on
992 equivalent fatigue load. Ocean Eng. 310, 118642 (2024).
993 https://doi.org/10.1016/j.oceaneng.2024.118642
994 9. Dai, S., Chaudhary, S.U.R., Wang, Y., Majig, G., Su, M., Zhang, X.: Delamination-induced buckling
995 and brittle failure of carbon fibre reinforced polymer (CFRP) laminates in wind turbine blades. Thin-
996 Walled Struct. 220, 114318 (2026). https://doi.org/10.1016/j.tws.2025.114318
997 10. Short, G.J., Guild, F.J., Pavier, M.J.: The effect of delamination geometry on the compressive failure
998 of composite laminates. Compos. Sci. Technol. 61, 2075–2086 (2001).
999 https://doi.org/10.1016/S0266-3538(01)00134-8
1000 11. Calvo, J.V., Feito, N., Miguélez, M.H., Giner, E.: Modeling the delamination failure under
1001 compressive loads in CFRP laminates based on digital image correlation analysis. Compos. Struct.
1002 287, 115265 (2022). https://doi.org/10.1016/j.compstruct.2022.115265
1003 12. Zhang, Y., Huang, K., Sun, R., Liao, F., Guo, L., Zhang, L.: Effect of embedded delamination on the
1004 compression performance of carbon fiber reinforced composites. Compos. Struct. 281, 115063
1005 (2022). https://doi.org/10.1016/j.compstruct.2021.115063
1006 13. Li, Y., Wang, B., Zhou, L.: Study on the effect of delamination defects on the mechanical properties
1007 of CFRP composites. Eng. Fail. Anal. 153, 107576 (2023).
1008 https://doi.org/10.1016/j.engfailanal.2023.107576
1009 14. Du, J., Tian, K., Cui, J., Hao, P.: Compressive behavior of composite laminates after multiple impacts:
1010 Effects of impact energy combinations and layup configurations. Compos. Struct. 381, 120066
1011 (2026). https://doi.org/10.1016/j.compstruct.2026.120066
1012 15. Köllner, A.: Predicting buckling-driven delamination propagation in composite laminates: An

analytical modelling approach. Compos. Struct. 266, 113776 (2021). https://doi.org/10.1016/j.compstruct.2021.113776

16. Shabanijafroudi, N., Ganesan, R.: A new methodology for buckling, postbuckling and delamination growth behavior of composite laminates with delamination. Compos. Struct. 268, 113951 (2021). https://doi.org/10.1016/j.compstruct.2021.113951

17. Venkat, S.S., Scheffler, S., Anilkumar, P.M., Baranger, E., Rolfes, R.: Effect of delamination defects on buckling and growth characteristics in composite laminates. Compos. Struct. 369, 119245 (2025). https://doi.org/10.1016/j.compstruct.2025.119245

18. Hwang, S.-F., Liu, G.-H.: Buckling behavior of composite laminates with multiple delaminations under uniaxial compression. Compos. Struct. 53, 235–243 (2001). https://doi.org/10.1016/S0263-8223(01)00007-1

19. Wang, X.W., Pont-Lezica, I., Harris, J.M., Guild, F.J., Pavier, M.J.: Compressive failure of composite laminates containing multiple delaminations. Compos. Sci. Technol. 65, 191–200 (2005). https://doi.org/10.1016/j.compscitech.2004.06.010

20. Jin, F., Xu, P., Xia, F., Liang, H., Yao, S., Xue, J.: Buckling of composite laminates with multiple delaminations: Part I: Theoretical and numerical analysis. Compos. Struct. 250, 112491 (2020). https://doi.org/10.1016/j.compstruct.2020.112491

21. Zhu, Z., Yang, P., Xia, F., Jin, F., Liang, H., He, Z., Xue, J.: Buckling of composite laminates with multiple delaminations: Part II: Experiments. Compos. Struct. 247, 112498 (2020). https://doi.org/10.1016/j.compstruct.2020.112498

22. De Carvalho, N.V., Ratcliffe, J.G.: Simulating delamination growth accounting for fracture directionality using a cohesive element approach. Compos. Part A Appl. Sci. Manuf. 172, 107619 (2023). https://doi.org/10.1016/j.compositesa.2023.107619

23. Vogler, M., Rolfes, R., Camanho, P.P.: Modeling the inelastic deformation and fracture of polymer composites – Part I: Plasticity model. Mech. Mater. 59, 50–64 (2013). https://doi.org/10.1016/j.mechmat.2012.12.002

24. Ding, J., Zhang, L., Li, Z., Zheng, T., Huang, K., Guo, L.: A 3D objective material model for elastic–plastic damage behavior of fiber reinforced polymer composites. Compos. Part A Appl. Sci. Manuf. 175, 107804 (2023). https://doi.org/10.1016/j.compositesa.2023.107804

25. Teixeira Goncalves, P., Arteiro, A., Rocha, N., Otero, F.: Modeling 3D transverse elasto-plastic damage of unidirectional fiber-reinforced polymer composites using a smeared crack approach. Int. J. Solids Struct. 286–287, 112568 (2024). https://doi.org/10.1016/j.ijsolstr.2023.112568

26. Harrell, T.M., Thomsen, O.T., Dulieu-Barton, J.M.: Predicting the effect of lightning strike damage on the structural response of CFRP wind blade sparcap laminates. Compos. Struct. 308, 116707 (2023). https://doi.org/10.1016/j.compstruct.2023.116707